JGR Solid Earth

RESEARCH ARTICLE
10.1029/2022JB025274

Single-Crystal Elasticity of Phase E at High Pressure and Temperature: Implications for the Low-Velocity Layer Atop the 410-km Depth

Baoyun Wang[1,2,3], Yanyao Zhang[3], Suyu Fu[3], Xing Ding[1,4], Wen Liang[3,5], Eiichi Takahashi[1,4], Li Li[1,4], Sergey N. Tkachev[6], Vitali B. Prakapenka[6], Jung-Fu Lin[3], and Maoshuang Song[1,4]

[1]State Key Laboratory of Isotope Geochemistry, Guangzhou Institute of Geochemistry, Chinese Academy of Sciences, Guangzhou, China, [2]College of Earth and Planetary Sciences, University of Chinese Academy of Sciences, Beijing, China, [3]Department of Geological Sciences, Jackson School of Geosciences, The University of Texas at Austin, Austin, TX, USA, [4]CAS Center for Excellence in Deep Earth Science, Guangzhou, China, [5]Key Laboratory of High Temperature and High Pressure Study of the Earth's Interior, Institute of Geochemistry, Chinese Academy of Sciences, Guiyang, China, [6]Center for Advanced Radiation Sources, University of Chicago, Chicago, IL, USA

Abstract Dense hydrous magnesium silicate (DHMS) phase E is a potential water carrier in subducting slabs that can transport water to the Earth's deep mantle between the bottom of the upper mantle and the uppermost transition zone. Therefore, knowledge on the high pressure–temperature (*P–T*) full elastic moduli of phase E at relevant mantle conditions is important in deciphering the existence of DHMS phases and their influences on seismic profiles in the region; however, the high *P–T* elasticity data of phase E still remains lacking. In this work, we determined the combined effect of *P–T* on the single-crystal elasticity of phase E up to 24 GPa and 900 K by in situ X-ray diffraction and Brillouin scattering measurements in externally-heated diamond anvil cells. The aggregate elastic moduli and compressional-wave (V_P) and shear-wave (V_S) velocities of phase E are then derived by analyzing the single-crystal elasticity and density data using the third-order finite-strain equations. We found that phase E exhibits much lower bulk and shear moduli and acoustic velocities than the most abundant constituent minerals in the upper mantle and transition zone, such as olivine, clinopyroxene, garnet, and wadsleyite. The modeled results using the obtained elasticity results show that the existence of phase E in a hydrated pyrolite model can result in relatively lower *Vp* and *Vs* profiles and negative velocity anomalies in seismic observations. The existence of phase E with relatively lower velocity profiles could be a possible origin of the low-velocity layers atop the 410-km discontinuity in some cold and highly-hydrated regions.

Plain Language Summary Deep-mantle water storage and circulation remains one of the most intriguing issues in geoscience. Serpentine and its high pressure–temperature (*P–T*) phases, namely high-density magnesium silicates (phases A, superhydrous B, D, E, and H), are considered to be the dominant potential water carriers in subduction zones. Hence, their sound velocities and density at high *P–T* conditions are of particular importance for interpreting seismic observations and understanding water circulation and geodynamic processes in subduction-related environments. In this study, we report new experimental results on the high *P–T* single-crystal elasticity of phase E up to 24 GPa and 900 K obtained by in situ synchrotron X-ray diffraction and Brillouin scattering measurements. The single-crystal elasticity data of phase E are used to derive its aggregate sound velocities and build mantle velocity profiles for dry and hydrated pyrolite models. We found that the existence of phase E in a hydrated pyrolite model can result in relatively lower compressional-wave and shear-wave velocity profiles and negative velocity anomalies in seismic observations. This finding helps explain the origin of the low-velocity layers atop the 410-km discontinuity in some highly-hydrated regions.

Key Points:

- Single-crystal elasticity of the Mg-endmember phase E has been measured at high pressure and temperature conditions
- The aggregate sound velocities of phase E are much lower than those of the typical minerals in the upper mantle and mantle transition zone
- The existence of phase E could contribute to the origin of the low-velocity layers atop the 410 km discontinuity in some hydrated regions

Supporting Information:

Supporting Information may be found in the online version of this article.

Correspondence to:

J.-F. Lin and M. Song,
afu@jsg.utexas.edu;
msong@gig.ac.cn

Citation:

Wang, B., Zhang, Y., Fu, S., Ding, X., Liang, W., Takahashi, E., et al. (2022). Single-crystal elasticity of phase E at high pressure and temperature: Implications for the low-velocity layer atop the 410-km depth. *Journal of Geophysical Research: Solid Earth*, *127*, e2022JB025274. https://doi.org/10.1029/2022JB025274

Received 1 AUG 2022
Accepted 17 NOV 2022

Author Contributions:

Conceptualization: Jung-Fu Lin, Maoshuang Song
Formal analysis: Baoyun Wang, Yanyao Zhang
Funding acquisition: Jung-Fu Lin, Maoshuang Song
Investigation: Baoyun Wang, Yanyao Zhang, Suyu Fu, Wen Liang, Eiichi Takahashi
Project Administration: Jung-Fu Lin, Maoshuang Song
Resources: Xing Ding, Eiichi Takahashi, Li Li, Sergey N. Tkachev, Vitali B. Prakapenka, Jung-Fu Lin
Visualization: Baoyun Wang, Suyu Fu
Writing – original draft: Baoyun Wang
Writing – review & editing: Jung-Fu Lin, Maoshuang Song

1. Introduction

A number of seismological studies have revealed a low-velocity layer with a thickness of ~20–90 km atop the 410 km discontinuity (410-LVL) beneath some subduction zones and Precambrian continental platforms (e.g., Han et al., 2020; Revenaugh & Sipkin, 1994; Tauzin et al., 2017; Vinnik & Farra, 2007). The low-velocity layers are characterized by 1.0%–5.0% and 1.5%–6.5% reductions in compressional-wave and shear-wave velocities (V_P and V_S), respectively (Fan et al., 2020). Several genesis mechanisms have been proposed to explain the

seismic velocity anomaly of the 410-LVL, including partial melting (Han et al., 2020; Sun et al., 2020; Thomson et al., 2016), thermal anomaly (Obayashi et al., 2006; Tang et al., 2014; Vinnik & Farra, 2007), and compositional heterogeneity (Fan et al., 2020; Lee, 2003). Among these mechanisms, water-induced partial melting has often been taken as the plausible cause of the 410-LVL in tectonic settings where water is enriched, such as the mantle transition zone with stagnant slabs or the mantle wedge above a subducted slab (Han et al., 2020; Tauzin et al., 2017; Wei & Shearer, 2017). Observations of natural hydrous ringwoodite and ice-VII inclusions in ultradeep diamonds have provided further evidence that water can be enriched at least in some regions of the mantle transition zone (Pearson et al., 2014; Tschauner et al., 2018).

It is widely accepted that water is mainly carried by hydrous minerals in subducted slabs in subduction zones and can be transported to the Earth's deep mantle (Ohtani, 2020). Based on phase-equilibrium studies of various slab components and geological observations of ancient subduction zones, a number of hydrous minerals have been identified as stable at high *P*–*T* conditions in subduction zones (e.g., Duan et al., 2018; Ohtani, 2020; Schmidt & Poli, 1998). Serpentine is the most abundant hydrous mineral in the ultramafic layer of a subducted slab and undergoes a sequence of phase transitions into dense hydrous magnesium silicates (DHMS, including phases A, superhydrous B (shy-B), D, E and H) along subducting depths. While the process of the aforementioned phase transitions can also release some of the water, the DHMS phases are found to be stable in the subduction zone conditions (Iwamori, 2004; Kawamoto et al., 1995; Komabayashi et al., 2004; Litasov & Ohtani, 2003; Ohtani, 2020). Therefore, serpentine and DHMS phases can be considered as the major potential water carriers in subduction zones, forming a continuous chain of water transport from the Earth's surface to the middle of the lower mantle. The DHMS phases have a relatively high-water content and hydrogen bonds in their crystal structures in comparison with the nominally anhydrous minerals of the constituent mantle phases. The high-water content in the DHMS phases contributes to their unique physical properties including the sound velocities and rheology (Mookherjee & Tsuchiya, 2015; Tsuchiya & Tsuchiya, 2008; Wang et al., 2022). Thus, determining the elastic properties of the DHMS phases, particularly at the high *P*–*T* conditions of the mantle is important to decipher the related seismic anomalies, to evaluate the potential storage sites, distribution and circulation of water in subduction zones and to deepen our understanding of the subduction-related geochemical and geodynamic processes (Duan et al., 2018; Karato, 2011; Karato et al., 2020; Li et al., 2016; Rosa et al., 2012; Xu et al., 2020). Several high-pressure experimental studies on elasticity have been reported for some DHMS phases, and the results obtained for phases shy-B and D have been used to explain the seismic anomalies in the mantle transition zone and the uppermost part of the lower mantle (Li et al., 2016; Rosa et al., 2012; Xu et al., 2020).

Phase E is a key member of the DHMS family which has been found to be stable at 10–18 GPa and 700°C–1100°C, corresponding to the *P*–*T* conditions of subducted slabs at the depths of 300–520 km in several experimental phase relation studies of the MgO-SiO_2-H_2O system and H_2O-saturated peridotites (Frost & Fei, 1998; Iwamori, 2004; Kanzaki, 1991; Komabayashi et al., 2004; Ohtani et al., 2004). In addition, (Fe, Al)-bearing phase E was synthesized under *P*–*T* conditions near the normal mantle geotherm in hydrous KLB-1 peridotite, implying that Fe and Al incorporation can expand the stability field of phase E to stabilize it under the mantle geotherm (Kawamoto et al., 1995; Zhang et al., 2019). Thus far, these phase stability studies have indicated that as much as 50% of phase E (an upper bound) could be accommodated in the fully hydrated mantle conditions between the bottom of the upper mantle and the topmost transition zone (Ohtani et al., 2004). To decipher the seismological observations and determine the role of phase E in the water circulation in subduction zones as well as in low-velocity seismic anomalies, such as the 410-LVL, high *P*–*T* elastic properties of phase E, particularly single-crystal elasticity, are essential. To date, only the equations of state at high pressure and single-crystal elasticity under ambient conditions have been reported for phase E.

Phase E has trigonal symmetry and crystallizes in the rhombohedral space group $R\bar{3}m$; its structure consist of brucite-like octahedral layers with tilted O-H dipoles that are cross-linked by statistically distributed Si-tetrahedra and Mg-octahedra (Kudoh et al., 1993; Tomioka et al., 2016). It has a nonstoichiometric formula depending on the hydrogen content and composition, and the Mg-endmember has a general chemical formula of $Mg_{3-0.5x}Si_xH_{6-3x}O_6$, where x varies between 1 and 1.3, with a H_2O storage capacity of 11–18 wt% (Purevjav et al., 2020; Tomioka et al., 2016). Two previous X-ray diffraction (XRD) studies reported an isothermal bulk modulus of K_{T0} = ~93 GPa and its pressure derivative of K'_{T0} = 5(1) for both iron-free and iron-bearing phase E (Crichton & Ross, 2000; Shieh et al., 2000). Recent Brillouin scattering measurements on iron-bearing single-crystal phase E ($Mg_{2.12}Fe^{2+}_{0.16}Fe^{3+}_{0.05}Ni_{0.01}Si_{1.12}O_6H_{2.67}$) under ambient conditions determined an adiabatic bulk modulus of K_{S0} = 95.9(4) GPa and an adiabatic shear modulus of G_0 = 59.6(2) GPa (Satta et al., 2019), which are markedly

lower than those of the representative constituent minerals in the upper mantle and the mantle transition zone (e.g., Fan et al., 2020; Irifune et al., 2008; Katsura et al., 2009; Mao et al., 2015; Wang et al., 2014). The low values of the adiabatic bulk and shear moduli for phase E imply that phase E has relatively low compressional-wave and shear-wave velocities, which could contribute to a detectable low-velocity seismic signature in hydrated regions of the mantle where a significant amount of phase E is present.

In this work, we performed in situ XRD and Brillouin light scattering (BLS) measurements on single-crystal phase E up to 24 GPa and 900 K to determine its high *P–T* equation of state and full elastic tensor. Using the obtained single-crystal elasticity data, we have derived the anisotropy factors and aggregate compressional-wave and shear-wave velocities of phase E at high *P–T* conditions relevant to a subducting slab. These results are used to model the velocity profiles of a hydrated pyrolite mantle model with ~13% phase E and to compare with a dry pyrolite model and seismic profiles of the regions (the lowest upper mantle and the upper transition zone). Our results reveal that the existence of phase E in the mantle can lead to relatively lower *Vp* and *Vs* profiles that are consistent with the seismic signatures of the 410-LVLs.

2. Experimental Methods

The starting material for the synthesis of single-crystal phase E was a ground mixture of $Mg(OH)_2$ and SiO_2 in a 2:1 M ratio. The mixture was sealed in a Pt capsule of 2 mm in diameter and 2.5 mm in length, which was then placed in a 14/8 sample assembly (a 14 mm edge length of the MgO octahedron [pressure medium] and 8 mm truncations of tungsten carbide anvils). The synthesis was performed at 14 GPa and 1000°C for a duration of 14 hr using the Sakura 2500-ton multi-anvil apparatus at the Guangzhou Institute of Geochemistry, Chinese Academy of Sciences. The recovered product was composed of well-crystallized transparent single crystals with a maximum size of ~500 μm. Single-crystal XRD analysis confirmed that these single crystals were phase E with the $R\bar{3}m$ symmetry and ambient lattice parameters $a = 2.968(1)$ Å and $c = 13.855(2)$ Å, and $V_0 = 105.95(3)$ Å^3. The chemical composition of several crystals was analyzed using an electron microprobe at the Guangzhou Institute of Geochemistry, Chinese Academy of Sciences, showing that the crystals were chemically homogenous with an average composition of 40.5(1) wt% SiO_2 and 47.6(1) wt% MgO. With the H_2O content being estimated from the weight deficiency in the analysis totals, the mineral formula of the synthesized phase E is determined to be $Mg_{2.22(1)}Si_{1.27(2)}H_{2.48(1)}O_6$, and the calculated density is 2.949(1) g/cm^3.

High *P–T* BLS and XRD experiments were conducted on selected phase E crystal platelets at the 13-BMD beamline of GSECARS, Advanced Photon Source (APS), Argonne National Laboratory (Sinogeikin et al., 2006). High *P–T* conditions were generated using BX90-type externally-heated diamond-anvil cells (EHDAC) with an alumina heater coiled with platinum wires (Kantor et al., 2012; Lu et al., 2013; Yang et al., 2014). The culets of the diamond anvils were 300 and 500 μm in diameter. The sample, Au pressure calibrant and neon pressure medium were loaded into the sample chamber, which was drilled as a hole with a diameter of approximately 2/3 of the culet size in a pre-indented Re gasket. The temperature of the sample was determined by an *R*-type thermocouple that was attached to the surface of one diamond anvil ~500 μm away from its culet and covered by thermally conductive ceramics. We performed one complementary series of BLS experiments at high pressure and room temperature using a short-symmetry DAC at the Mineral Physics Laboratory, University of Texas at Austin (UT Austin), following experimental procedures described in the literature (Fan et al., 2019; Fu et al., 2019; Yang et al., 2016; Zhang et al., 2021). To determine the density of phase E for the room-temperature BLS experiments, an additional run of XRD measurements at high pressures and room temperature was also performed at the 13-IDD beamline of GSECARS. For the room-temperature BLS experiments, the pressures were determined using a ruby pressure calibrant which is internally consistent with the Au pressure calibrant used in high *P–T* BLS experiments (Fei et al., 2007).

During XRD measurements in 13-BMD or 13-IDD beamline of GSECARS, each XRD pattern was obtained for phase E crystal platelets and Au pressure calibrants by integrating images collected in the single-crystal wide-scan mode or step-scan (1° per step) from −15° to +15°. In both beamlines, the X-ray beam energy was 37 keV (0.3344 Å in wavelength) and a stationary Perkin-Elmer image plate was used as the detector. The diffraction geometry parameters were calibrated using the LaB_6 standard. The obtained diffraction patterns were converted into one-dimensional profiles using DIOPTAS (Prescher & Prakapenka, 2015), which were then indexed by UNITCELL software to retrieve the lattice parameters at each given *P–T* point (Holland & Redfern, 1997). A representative integrated XRD pattern of phase E at 22.6 GPa and 300 K is shown in Figure 1a.

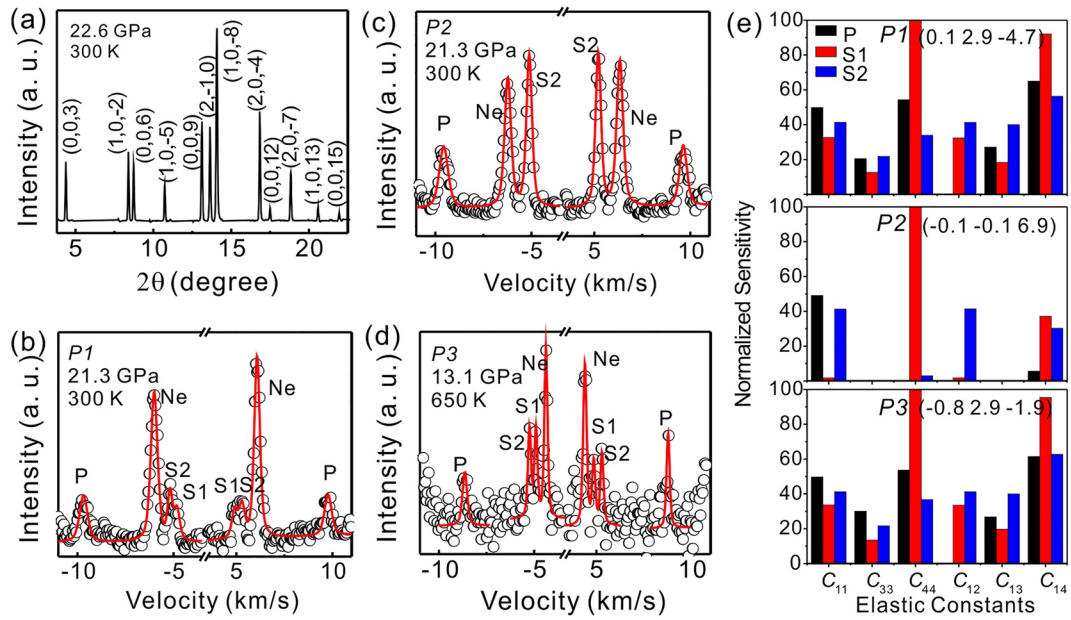

Figure 1. X-ray diffraction (XRD) and sound velocity measurements of phase E at high pressures. (a) An integrated XRD pattern of phase E with indexed diffraction peaks at 22.6 GPa and 300 K. (b–d) Representative Brillouin scattering spectra for platelets P1 (0.1 2.9 −4.7) and P2 (−0.1 −0.1 6.9) at 21.3 GPa and 300 K, and P3 (−0.8 2.9 −1.9) at 13.1 GPa and 650 K. P, S1, S2, and Ne denote the V_P, V_{S1}, and V_{S2} signals of phase E and the compressional-wave signal of neon, respectively. Black open circles are raw data and red lines are fitting results. (e) Sensitivity analyses of C_{ij} to the compressional-wave velocity V_P and shear-wave velocities V_{S1} and V_{S2} of phase E for the three platelets. The highest sensitivity of C_{44} in each platelet is set to 100% to normalize the sensitivity values of the other elastic moduli. Platelet P1 and platelet P3 are sensitive to all six elastic moduli with relatively high sensitivity values, while platelet P2 is not as sensitive to C_{33} and C_{13}.

Phase E with the trigonal $R\bar{3}m$ symmetry has six independent single-crystal elastic stiffness coefficients (C_{ij}s) or elastic moduli (Nye, 1985). To obtain reliable data for all six single-crystal elastic moduli, high *P–T* experiments and data analysis must be carefully designed. To start with, we double-polished a number of phase E crystals to platelets with a thickness of ∼15 μm. The crystallographic orientations of the platelets were measured by single-crystal XRD at the 13-IDD beamline of GSECARS. We then selected three platelets (P1, P2, and P3) with the determined crystallographic planes of P1 (0.1 2.9 –4.7), P2 (−0.1 −0.1 6.9) and P3 (−0.8 2.9 −1.9) in the Cartesian coordinate system for the Brillouin scattering measurements. The sensitivity tests of these three platelets indicated that platelets P1 and P3 were highly sensitive to all six single-crystal elastic moduli and can be used to retrieve the full single-crystal elastic tensor of phase E, whereas platelet P2 was used to provide additional constraints on the derivation of the single-crystal elastic moduli (see Figure 1e and Text S1 in Supporting Information S1; Lin et al., 2018). The compressional and shear wave velocities of all three platelets as a function of azimuthal angle (i.e., the angle of rotation around an axis normal to the platelet face) were collected in BLS measurements under ambient conditions to tightly constrain the ambient single-crystal elastic moduli of phase E. For high-pressure BLS experiments at ambient temperature (300 K), we loaded P1 and P2 together in the short-symmetry DAC and collected the spectra at UT Austin (Fu et al., 2017, 2019). Only P3 was loaded in a BX90-type EHDAC for high *P–T* BLS and XRD experiments at the 13-BMD beamline of GSECARS. The BLS and XRD experimental system at the 13-BMD beamline allowed us to collect both BLS spectra and XRD patterns in situ at high *P–T* to simultaneously determine the acoustic velocities and the density of sample for the derivation of the elastic moduli (Sinogeikin et al., 2006). BLS spectra were measured in a symmetric forward scattering geometry, in which acoustic velocities (ν) were calculated from the measured Brillouin shifts ($\Delta\upsilon_B$) using the following equation:

$$\nu = \frac{\Delta\upsilon_B \lambda_0}{2\sin(\theta/2)} \quad (1)$$

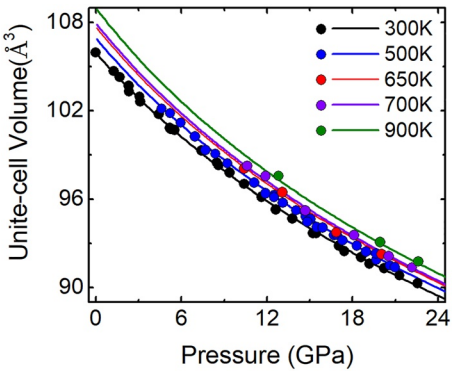

Figure 2. Unit-cell volumes of phase E at high *P–T* conditions. Solid circles are the experimental data obtained by X-ray diffraction measurements, and solid lines are fitting results using the third-order thermal Birch–Murnaghan equation of state (Birch, 1947; Zhang & Kostak, 2002). Black, blue, red, purple and olivine denote 300, 500, 650, 700, and 900 K, respectively.

where the scattering angle (θ) is 48.3° for the BLS system at UT and 50° for the BLS system at 13-BMD. The laser wavelength (λ_0) is 532 nm for both systems. Typical BLS spectra under high *P–T* conditions are shown in Figures 1b–1d.

3. Results and Data Analysis

3.1. Thermal Equation of State of Phase E

XRD patterns of single-crystal phase E and polycrystal Au were collected at high pressures up to 22.6 GPa and temperatures of 300, 500, 650, 700, and 900 K. The collected XRD patterns were converted into one-dimensional XRD profiles, which were then indexed and analyzed to derive the unit-cell parameters (Table S1 in Supporting Information S1). Pressures were calculated using the Au pressure scale of Fei et al. (2007). The obtained unit-cell volumes at the various *P–T* conditions are plotted in Figure 2.

The pressure–volume (*P–V*) data at the ambient temperature (300 K) were fitted with the third-order Birch–Murnaghan (BM) equation of state (Birch, 1947) that is expressed as follows:

$$P = \frac{3K_{T0}}{2}\left[\left(\frac{V}{V_0}\right)^{-7/3} - \left(\frac{V}{V_0}\right)^{-5/3}\right]\left\{1 + \frac{3}{4}\left(K'_{T0} - 4\right)\left[\left(\frac{V}{V_0}\right)^{-2/3} - 1\right]\right\} \quad (2)$$

where V_0, $K_{T0,}$ and K'_{T0} are the zero-pressure unit-cell volume, ambient isothermal bulk modulus and its pressure derivative, respectively. With a fixed $V_0 = 105.95(3)$ Å^3, the best fitting yielded the values of $K_{T0} = 94.7(1.3)$ GPa and $K'_{T0} = 4.73(21)$. These results are in good agreement with the results obtained in a previous study on phase E by Shieh et al. (2000).

To obtain the thermal elastic parameters of phase E, the high-temperature *P–V* data were analyzed with the high-temperature Birch–Murnaghan (HTBM) equation of state (Birch, 1947; Zhang & Kostak, 2002). The HTBM equation of state is in the same form as Equation 2, except that V_0, $K_{T0,}$ and K'_{T0} are replaced with V_{T0}, K_T, and K'_T, which are the zero-pressure unit-cell volume, isothermal bulk modulus and its pressure derivative at a constant temperature *T*, respectively. K_T and V_{T0} can be related to the ambient temperature K_{T0} and V_0 by the following expressions:

$$K_T = K_{T0} + (\partial K_T/\partial T)_P\,(T - 300) \quad (3)$$

$$V_{T0} = V_0 \exp\left[\int_{300}^{T} \alpha_T \mathrm{d}T\right] \quad (4)$$

where $(\partial K_T/\partial T)_P$ and α_T are the temperature derivative of the isothermal bulk modulus and thermal expansion of the volume, respectively. Within the limited temperature range of our high *P–T* experiments, we assumed two approximations, namely $\alpha_T = \alpha_0$ (thermal expansion at ambient temperature) and $K'_T = K'_{T0}$ in the analysis (Nishihara et al., 2003). Coupled with the obtained V_0, K_{T0}, and K'_{T0} values at ambient temperature, fitting the *P–V–T* data at 500, 650, 700, and 900 K together yielded $(\partial K_T/\partial T)_P = -0.014(3)$ GPa/K and $\alpha_0 = 4.7(4) \times 10^{-5}$ K^{-1}. The obtained thermal equation of state parameters of phase E match our *P–V–T* experimental data well (Figure 2), supporting the assumptions used in the modeling.

3.2. Single-Crystal Elastic Moduli (C_{ij}s) of Phase E at High *P–T* Conditions

BLS measurements on phase E were performed at high pressures up to 24 GPa and temperatures of 300, 500, and 650 K (Figures 1b–1c). All three platelets were used for BLS measurements under ambient conditions, while platelets P1 and P2 were used for high-pressure and ambient-temperature BLS measurements and platelet P3 was used for high *P–T* BLS measurements. At given *P–T* conditions, the acoustic wave velocities were collected with an interval of 10° azimuthal angles over a range of 180° for each platelet (Figure 3). The density at high *P–T* was determined via analysis of the single-crystal XRD patterns before and after the Brillouin measurements, whereas

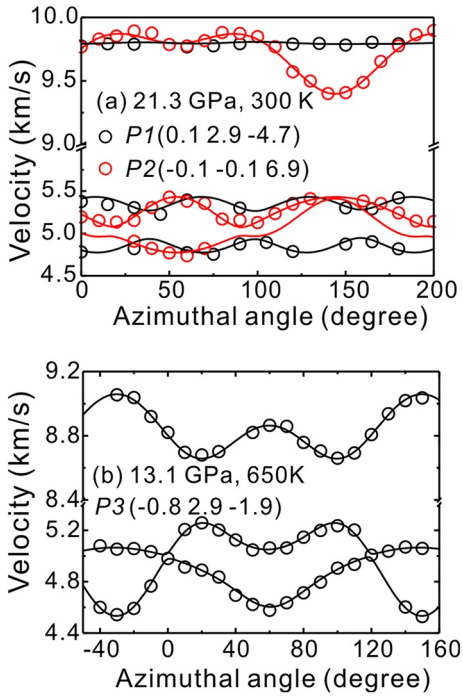

Figure 3. Compressional-wave and shear-wave velocities of single-crystal phase E as a function of azimuthal angles at high *P–T*. (a) Platelets P1 (red open circles) and P2 (black open circles) at 21.3 GPa and 300 K. (b) Platelet P3 at 13.1 GPa and 650 K. The solid lines are the velocities calculated from the derived single-crystal elastic moduli.

the density at high pressure and 300 K was calculated by the thermal equation of state as mentioned above. The experimental velocity data along various crystallographic directions were fitted by Christoffel's equation at each *P–T* point to obtain six single-crystal elastic moduli (Every, 1980):

$$|C_{ijkl}n_in_j - \rho v^2\delta_{kl}| = 0 \quad (5)$$

where C_{ijkl} are the elastic stiffness coefficients (or elastic moduli) with full suffix notation, v is the measured acoustic velocity, ρ is the density derived from single-crystal XRD measurements, n_i and n_j are the wave-vector (phonon propagation) direction cosines and δ_{kl} is the Kronecker delta. Representative fitting results of the single-crystal elastic moduli for P_1 and P_2 at 21.3 GPa and 300 K and P_3 at 13.1 GPa and 650 K are displayed in Figure 3, showing that the velocities determined by the BLS spectra agree well with the velocities calculated using the fitted single-crystal elastic moduli. All of the fitted single-crystal elastic moduli of phase E at various *P–T* conditions are given in Table S2 in Supporting Information S1 and plotted in Figure 4. Because the sign of C_{14} would be reversed when the *X-Y* axes are rotated by $(2n + 1) \times 60°$, the sign of C_{14} reported by Satta et al. (2019) was flipped for comparison in Table S2 in Supporting Information S1. Notably, such a treatment does not affect the physical interpretation and the values of other single-crystal elastic moduli. Our values under ambient conditions are roughly consistent with those of Satta et al. (2019), with the small differences interpreted as a result of the iron-substitution effects in phase E.

To obtain the *P–T* derivatives of the single-crystal elastic moduli, the experimental single-crystal elastic data were fitted using third-order finite-strain equations (Birch, 1978; Duffy & Anderson, 1989) (Figure 4 and Table S3 in Supporting Information S1):

$$C_{ij}(0, T) = C_{ij}(0, 300\,K) + (T - 300)\,(\partial C_{ij}/\partial T)_P \quad (6)$$

$$C_{ij}(P, T) = (1 + 2f)^{7/2}\left[C_{ij}(0, T) + a_1 f\right] + a_2 P \quad (7)$$

$$a_1 = 3K_T(0, T)\left[(\partial C_{ij}/\partial P)_T - a_2\right] - 7C_{ij}(0, T) \quad (8)$$

$$f = \left(\frac{1}{2}\right)\left[\left(\frac{V_0}{V}\right)^{\frac{2}{3}} - 1\right] \quad (9)$$

where C_{ij}(0,300 K) is the elastic modulus under ambient conditions; C_{ij}(0,*T*) is the elastic modulus at high temperature and ambient pressure; C_{ij}(*P*,*T*) is the elastic modulus at given *P–T* conditions; $(\partial C_{ij}/\partial T)_P$ and $(\partial C_{ij}/\partial P)_T$ are the isobaric temperature derivative and the isothermal pressure derivative of the elastic modulus, respectively; K_T(0,*T*) is the isothermal bulk modulus at high temperature and ambient pressure; f is the finite strain; V is the unit-cell volume determined by single-crystal XRD; and V_0 is the unit-cell volume under ambient conditions. The parameter a_2 is 3 for C_{11} and C_{33}, 1 for C_{44}, C_{12} and C_{13}, and 0 for C_{14}.

3.3. Aggregate Elastic Property of Phase E (*Ks*, *G*, *Vp* and *Vs*)

At each given *P–T* point, the aggregate adiabatic elastic moduli K_S and G were calculated using the derived single-crystal elastic moduli in the Voigt–Reuss–Hill average (Hill, 1952). Then, with the K_S at ambient conditions fixed to 98.3(7) GPa, we derived the *P–T* derivatives of the adiabatic bulk modulus (Figure 5 and Table S3 in Supporting Information S1) by fitting the *Ks* values at various *P–T* conditions using the following equations (Angel et al., 2014; Birch, 1978; Stixrude and Lithgow-Bertelloni, 2005):

$$K_S(0, T) = K_S(0, 300\,\mathrm{K}) + \left(\frac{\partial K_S}{\partial T}\right)_P (T - 300) \quad (10)$$

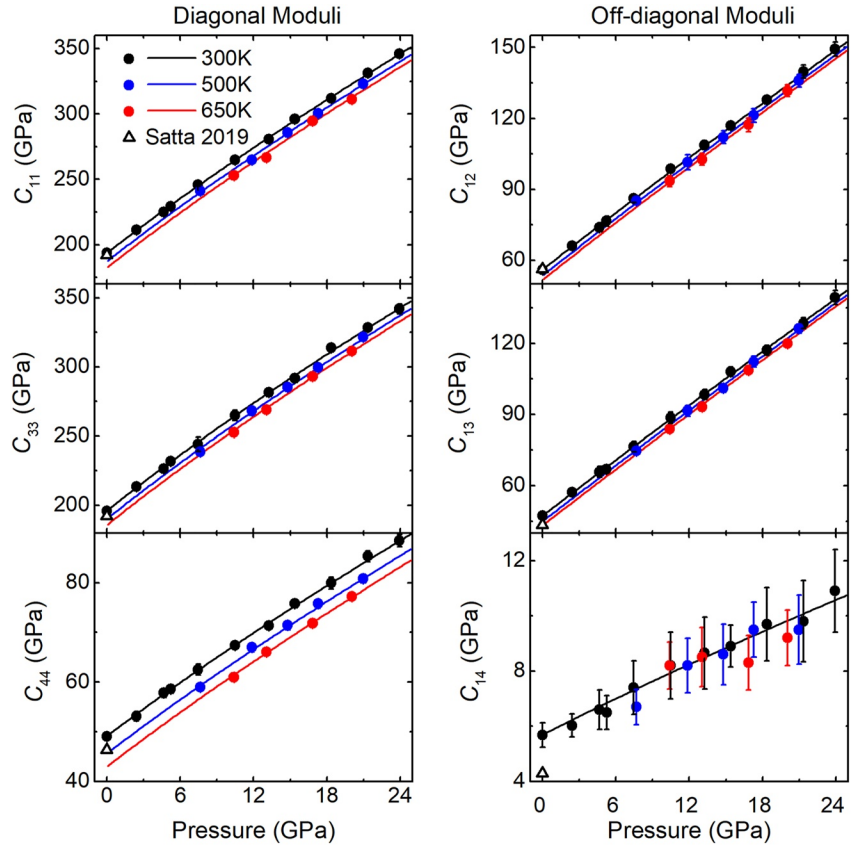

Figure 4. Single-crystal elastic moduli of phase E at high *P*–*T* conditions. Black, blue and red circles represent the experimental data at 300, 500, and 650 K, respectively. Solid lines are the fitting results obtained using thermal third-order finite strain equations (Birch, 1978). Open triangles are the results of iron-bearing phase E under ambient conditions from Satta et al. (2019). Vertical ticks show the error bars of the elastic moduli. Errors of the pressures are smaller than the symbols and are not shown.

$$K_S(P,T) = K_S(0,\,T)(1+2f)^{5/2}\left\{1+\left[3\left(\frac{\partial K_S}{\partial P}\right)_T - 5)\right]f + \left[\left(\frac{\partial K_S}{\partial P}\right)_T - 4\right]f^2\right\} \tag{11}$$

where $K_S(0,T)$ is the adiabatic bulk modulus at high temperature and ambient pressure, $K_S(P,\,T)$ is the adiabatic bulk modulus at given *P*–*T* conditions, $(\partial K_S/\partial T)_P$ is the temperature derivative of the adiabatic bulk modulus, and $(\partial K_S/\partial P)_T$ is the pressure derivative of the adiabatic bulk modulus. The derived *P*–*T* derivatives were 5.00(4) and −0.018(1) GPa/K for the adiabatic bulk modulus, respectively. Note that Equation 11 requires the assumptions $K_S(0,T) = K_T(0,T)$ and $(\partial K_S/\partial P)_T = (\partial K_T/\partial P)_T$.

Similarly, the *P*–*T* derivatives of the shear modulus were derived by fitting the *G* values at various *P*–*T* conditions using the following equations (Birch, 1978; Stixrude & Lithgow-Bertelloni, 2005) (Figure 5 and Table S3 in Supporting Information S1):

$$G(0,T) = G(0,300\,\mathrm{K}) + \left(\frac{\partial G}{\partial T}\right)_P (T-300) \tag{12}$$

$$\begin{aligned} G(P,T) = (1+2f)^{5/2}&\left\{G(0,T)\left[1+\left[3\left(\frac{\partial G}{\partial P}\right)_T - 5)f\right]\right]\right. \\ &\left.+\left[6K_S(0,\,T)\left(\frac{\partial G}{\partial P}\right)_T - 24\mathrm{K}(0,T) - 14G(0,T) + \frac{9}{2}K_S(0,\,T)\left(\frac{\partial K_S}{\partial P}\right)_T\right]f^2\right\} \end{aligned} \tag{13}$$

where $G(0,T)$ is the shear modulus at high temperature and ambient pressure, $G(P,T)$ is the shear modulus at given *P*–*T* conditions, $(\partial G/\partial T)_P$ is the temperature derivative of the shear modulus, and $(\partial G/\partial P)_T$ is the pressure

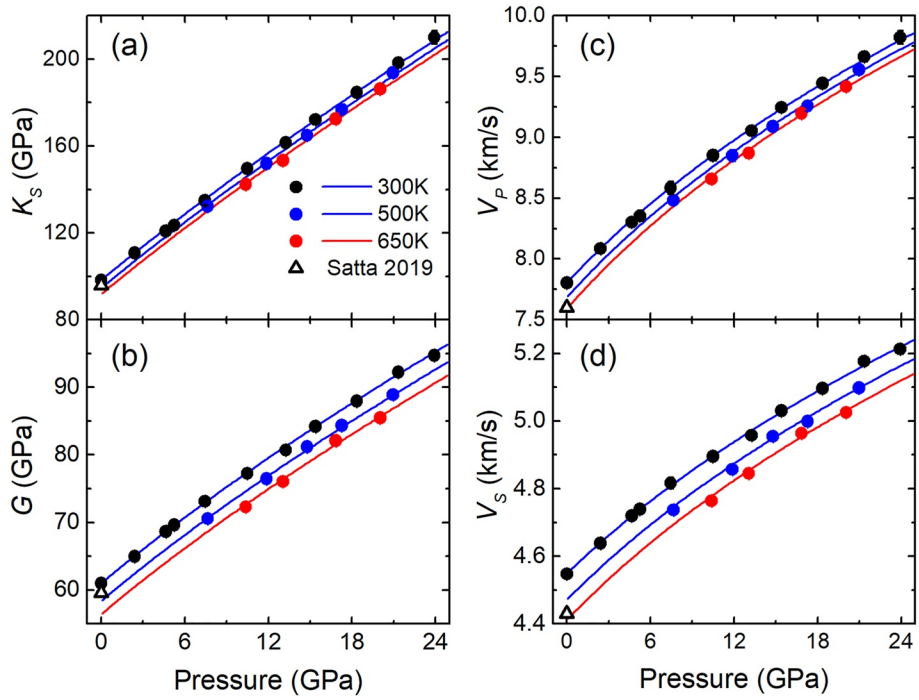

Figure 5. Aggregate elastic properties of phase E at high *P–T* conditions. (a and b) adiabatic bulk and shear moduli. (c and d) compressional-wave velocities and shear-wave velocities. Black, blue and red solid circles represent the experimental data at 300, 500, and 650 K, respectively. Solid lines are the fitting results obtained using third-order finite strain equations. Open triangles are the results of the iron-bearing phase E under ambient conditions from Satta et al. (2019). Most error bars are smaller than the symbols and are not shown.

derivative of the shear modulus. With a fixed G value of 61.0(1) GPa under ambient conditions, the pressure derivative and temperature derivative are 1.64(2) and −0.013(2) GPa/K for the shear modulus, respectively.

The aggregate V_P and V_S velocities of phase E were determined by the bulk and shear moduli (K_S, G) using the following equations:

$$V_P = \sqrt{\left(K_S + \frac{4}{3}G\right)/\rho} \tag{14}$$

$$V_S = \sqrt{G/\rho} \tag{15}$$

The calculated results at various *P–T* conditions are given in Table S2 in Supporting Information S1 together with the results at ambient conditions reported by Satta et al. (2019). Our V_P and V_S values under ambient conditions are 7.80(2) and 4.55(1) km/s, which are close to but slightly higher by ~2.7% than those obtained by Satta et al. (2019), possibly due to the difference in the chemical composition of phase E. Our velocity values are marginally consistent with those of Satta et al. (2019) within the reciprocal uncertainties, but we should note that the phase E sample used by Satta et al. (2019) contains 9.0 mol% iron so that the effects of iron substitution on the elasticity should be further considered in the comparison.

3.4. Anisotropic Factors of Phase E at High *P–T*

The V_P and V_S azimuthal anisotropies of phase E were analyzed by using its single-crystal elasticity data at high *P–T* conditions. We calculated the compressional-wave anisotropy factor (AV_P) and the shear-wave splitting anisotropy factor (AV_S) at each *P–T* point (Table S2 in Supporting Information S1), which are defined as follows (Karki et al., 2001; Mainprice et al., 2000):

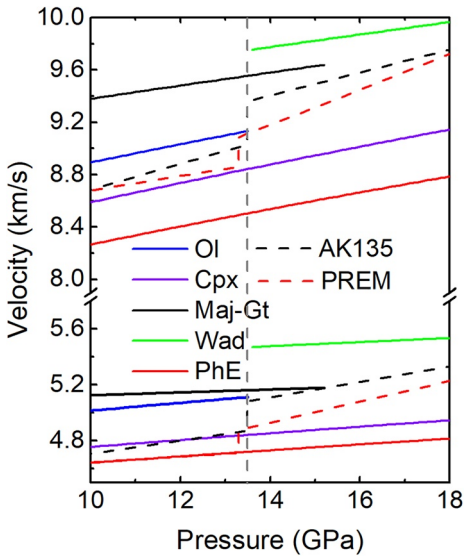

Figure 6. Modeled V_P and V_S profiles of phase E and other relevant mantle phases along a slab geotherm that is 400 K colder than the adiabatic temperature profile (Katsura et al., 2010). Blue solid lines: olivine (Ol, Mao et al., 2015); purple solid lines: clinopyroxene (Cpx, Fan et al., 2020); black solid lines: majorite (Maj-Gt, Irifune et al., 2008); green solid line: wadsleyite (Wad, Wang et al., 2014); red solid lines: phase E (PhE, this study). Black and red dashed lines show the seismic profiles of AK135 (Kennett et al., 1995) and PREM (Dziewonski & Anderson, 1981), respectively.

$$AV_P = 200 \times (V_{P\max} - V_{P\min}) \,/\, (V_{P\max} + V_{P\min}) \quad (16)$$

$$AV_S = 200 \times \left[(V_{S1} - V_{S2}) \,/\, (V_{S1} + V_{S2})\right]_{\max} \quad (17)$$

where $V_{P\max}$ and $V_{P\min}$ represent the maximum and minimum V_P velocities of the mineral, respectively, and V_{S1} and V_{S2} are two orthogonally polarized V_S velocities propagating along the same direction. Under ambient conditions, the AV_P and AVs values of phase E are 8.9% and 19.5%, respectively, which are close to those of iron-bearing phase E (Satta et al., 2019), implying that 9 mol% iron in phase E does not significantly affect the anisotropy under ambient conditions.

4. Discussion and Geophysical Implications

4.1. Elasticity of Phase E and Its Comparison With Relevant Mantle Minerals

Using the data obtained from Brillouin scattering spectroscopy and single-crystal XRD measurements, we have determined the single-crystal elasticity of the Mg-endmember phase E at high *P–T* conditions. Analysis of the elasticity data by the third-order finite-strain equations yields high *P–T* derivatives of all C_{ij}s, *Ks* and G, allowing us to extrapolate the elasticity data of phase E to the *P–T* conditions relevant to the upper mantle and the mantle transition zone. The C_{ij}s, aggregate K_S, and G under ambient conditions obtained in the present study, with the exception of C_{11}, $C_{12,}$ and C_{14}, are 2%–9% higher than the experimental results of Satta et al. (2019). These differences are most likely due to the effect of iron substitution for magnesium because phase E used in the BLS experiments of Satta et al. (2019) contained 9.0 mol% iron (Fe/(Mg + Fe) ratio). The longitudinal moduli, C_{11} and C_{12}, are not sensitive to iron substitution, while C_{14} appears to be highly sensitive. The effect of iron substitution on the elasticity (C_{ij}S, K_S, and G) has been studied for many minerals, such as olivine, diopside, wadsleyite, and bridgmanite (Fan et al., 2019, 2020; Fu et al., 2019; Wang et al., 2014). In many cases, the content of iron that substitutes magnesium shows a negative effect on the single-crystal elastic moduli, and especially on aggregate K_S, G, V_P, and V_S; that is, iron-bearing minerals have relatively lower single-crystal and aggregate elastic moduli than their iron-free counterparts.

A pyrolite model is usually employed to describe the chemical composition and mineralogy of the Earth's mantle. The phase relations of dry pyrolite in the Earth's mantle have been well constrained by high *P–T* experiments (Irifune & Isshiki, 1998; Ishii et al., 2011). According to the experimental studies on the phase relations of the hydrated pyrolite model and similar compositions (Kawamoto et al., 1995; Komabayashi et al., 2004; Litasov & Ohtani, 2003; Zhang et al., 2019), phase E could coexist with olivine, clinopyroxene and majorite in the lowest part of the upper mantle and with wadsleyite and majorite in the upper part of the mantle transition zone. A comparison of the elastic properties of phase E with its relevant (coexisting) mantle mineral phases could thus help us understand the potential effect of hydration with the existence of phase E on the seismic velocities and anisotropies in the Earth's upper mantle and the mantle transition zone. Using the thermoelastic parameters for phase E obtained in this study and the parameters for olivine, diopside, majorite and wadsleylite reported in the literature (See Table S4 in Supporting Information S1; Fan et al., 2020; Irifune et al., 2008; Isaak et al., 2006, 2010; Katsura et al., 2009; Mao et al., 2015; Pandolfo et al., 2015; Wang et al., 2014; Zou et al., 2012), we have modeled V_P and V_S velocity profiles of these minerals along a slab geotherm that is 400 K colder than the adiabatic temperature profile (Katsura et al., 2010). As shown in Figure 6, we found that both the V_P and V_S velocities of phase E are significantly lower than those of the other mineral phases. Phase E is ~7% lower in V_P and ~8% lower in V_S than olivine at the depth of the upper mantle and ~13% lower in V_P and ~14% lower in V_S than wadsleylite at the depth of the mantle transition zone. The low V_P and V_S velocities of phase E imply that it might be a potential cause for the low-velocity anomalies observed at the depths of the lowest part of the upper mantle and the upper part of the mantle transition zone in the water-rich tectonic settings related to slab subduction (Han et al., 2020; Zhao & Ohtani, 2009).

Using the obtained high *P–T* single-crystal elastic parameters of phase E, we have also calculated the compressional-wave anisotropy factor AV_P and shear-wave splitting anisotropy factor AV_S along a slab geotherm

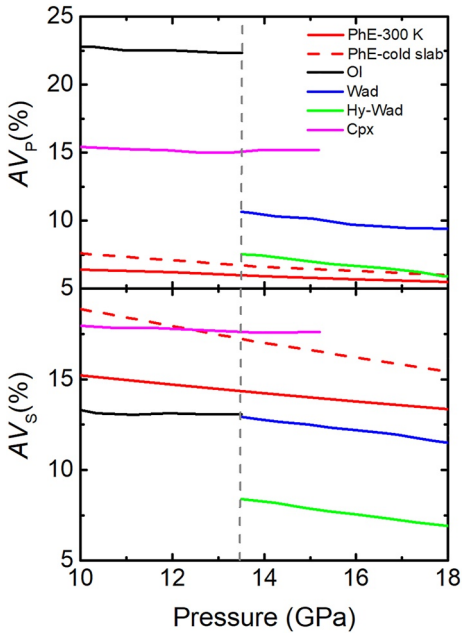

Figure 7. The anisotropy factors AV_P and AV_S of phase E and representative minerals in the upper mantle and the transition zone. The solid lines represent phase E (red lines, this study), olivine (black lines, Mao et al., 2015), wadsleyite (blue lines, Wang et al., 2014), hydrous wadsleyite (green lines, Zhang et al., 2018) and clinopyroxene (pink lines, Hao et al., 2020) as a function of pressure at 300 K. The red dashed lines represent the anisotropy factors of phase E along a slab geotherm that is 400 K colder than the adiabatic temperature profile (Katsura et al., 2010). The vertical gray dashed line marks the boundary between the upper mantle and the mantle transition zone.

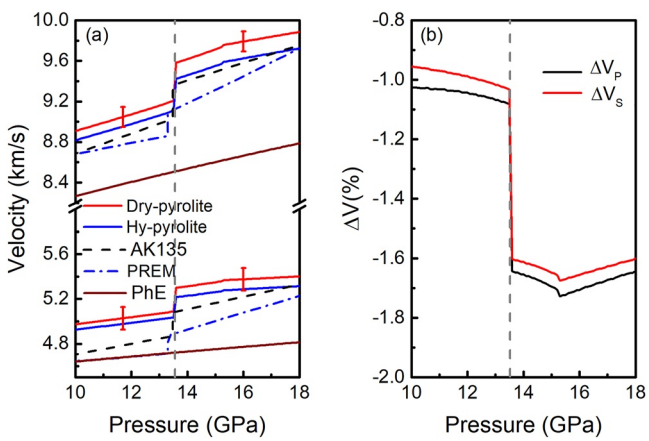

Figure 8. Comparison between the velocity profiles of a pyrolite model, phase E, and seismic models in the upper mantle and the transition zone. (a) Modeled velocity profiles of dry pyrolite (red lines) and hydrated pyrolite with ~13 vol% phase E (blue lines) and phase E (brown lines) along a slab geotherm that is 400 K colder than the adiabatic temperature profile (Katsura et al., 2010). Seismic profiles, AK135 (Kennett et al., 1995) and PREM (Dziewonski & Anderson, 1981), are shown as black and blue dashed lines, respectively. (b) The velocity contrast between dry and hydrous pyrolites ($\Delta V_{P,S} = 100 \times [(V_{P,S})_{\text{hydrous}} - (V_{P,S})_{\text{dry}}]/(V_{P,S})_{\text{dry}}$). The black and red lines are the compressional velocity contrast (ΔV_P) and shear velocity contrast (ΔV_S), respectively. The vertical gray dashed line marks the boundary between the upper mantle and the mantle transition zone.

400 K lower than the adiabatic temperature profile (Katsura et al., 2010) and as a function of pressure at 300 K, respectively (Figure 7). Both AV_P and AV_S show a decrease with pressure and an enhancement with temperature. Due to a lack of constraints on the effect of temperature on the single-crystal elasticity of clinopyroxene and wadsleylite, we only calculated the AV_P and AV_S of olivine, clinopyroxene and wadsleylite as a function of pressure at the ambient temperature using the literature single-crystal elasticity data (Hao et al., 2020; Mao et al., 2015; Wang et al., 2014; Zhang et al., 2018) for a comparison with phase E. Majorite was not included in the comparison because it is nearly elastically isotropic at high pressures and 300 K (Murakami et al., 2008; Sanchez-Valle et al., 2019). As seen in Figure 7, the AV_P of phase E is significantly lower than that of olivine, clinopyroxene and anhydrous wadsleylite but is comparable to that of hydrous wadsleyite. The AV_S of phase E is only lower than that of clinopyroxene but is higher than those of olivine, anhydrous wadsleyite and hydrous wadsleyite. The intrinsic elastic anisotropy of phase-E would produce a seismic signature in the case of texturing by lattice preferred orientation. Phase E with a relatively high AV_S may contribute to the shear-wave splitting anisotropy observed at the depth of the mantle transition zone in some subduction zones (Chang & Ferreira, 2019; Zhang et al., 2018).

4.2. Implications for the Low-Velocity Layers Atop the 410-km Depth

Seismic observations using mainly P and S receiver functions revealed the existence of a low-velocity layer atop the mantle transition zone in some subduction zones and continental platforms (Han et al., 2020; Li et al., 2022; Tauzin et al., 2017; Vinnik & Farra, 2007). A water-induced partial-melting model is often employed to interpret the origin of the 410-LVL (Kuritani et al., 2019; Tauzin et al., 2010, 2017). Water, which was predicted to be released through the upwelling of a hydrous mantle transition zone and dehydration reactions of a subducted slab or stagnant slab, has been proposed to result in partial melting that can significantly reduce the seismic velocities (V_P and V_S) in the lowest part of the upper mantle above the 410 km discontinuity. However, while the existence of water can induce partial melting, it may also lead to the formation of phase E, which is stable at the pressures of 10–18 GPa under slab geotherms and even under normal mantle geotherms (Kawamoto et al., 1995; Zhang et al., 2019). The low V_P and V_S velocities of phase E imply that it may contribute to the origin of the 410-LVL.

To evaluate the effect of phase E on the 401-LVL, we have modeled the velocity profiles of dry and hydrated pyrolite models as well as the profiles of phase E at the depths of 300–520 km corresponding to 10–18 GPa pressure range along a slab geotherm that is 400 K colder than the surrounding mantle geotherm (Katsura et al., 2010). The thermal elastic parameters of the minerals used for the modeling are listed in Table S4 in Supporting Information S1. The mineral assemblages and the proportions of the dry pyrolite model are taken from the experimental results of Irifune and Isshiki (1998) with the olivine or wadsleyite content fixed at ~60 vol% in the entire modeling pressure range. For hydrated pyrolite, the amount of phase E was added at the expense of olivine or wadsleyite, based on a previous study (Satta et al., 2019). According to the water content reported for a hydrous ringwoodite inclusion in an ultradeep diamond (Pearson et al., 2014), we assumed a H_2O content of 1.5 wt% for the hydrated pyrolite model, corresponding to ~13 vol% phase E. As depicted in Figure 8, the hydrated pyrolite model shows lower velocities than the dry pyrolite counterpart, while the

reductions in V_P and V_S, $\Delta V_{P,S} = 100*[(V_{P,S})_{\text{dry}} - (V_{P,S})_{\text{hydrous}}]/(V_{P,S})_{\text{dry}}$, are similar to each other. Both the V_P and V_S velocity profiles of phase E are ~8% lower than those of the dry pyrolite model (Figure 8a). Compared with the dry pyrolite model, phase E with ~13 vol% in the hydrated pyrolite model can lead to a decrease in both V_P and V_S by ~1.0% at the depth of the lowermost upper mantle and by ~1.6% at the depth of the mantle transition zone, respectively (Figure 8b). The modeled V_P and V_S profiles of phase E are much lower than those of AK135 and PREM; hence, it is expected that the enrichment of phase E in the hydrous regions of the lowest part of the upper mantle and the mantle transition zone can lead to a negative seismic anomaly. We note that the modeled velocity profiles of the dry and hydrated pyrolite models are slightly higher than those of the AK135 and PREM models (Dziewonski & Anderson, 1981; Kennett et al., 1995), which is most likely due to the lower temperature of the selected slab geotherm. The use of the elasticity of the Mg-endmember phase E in the present modeling calculations may also overestimate the V_P and V_S profiles. In the pyrolite model, phase E should contain some amounts of iron and aluminum, which can significantly reduce the aggregate elastic moduli and acoustic velocities of phase E (Satta et al., 2019; Xu et al., 2020).

A number of evidences from high *P–T* experiments and geophysical and geological observations indicate that at least in some regions, the mantle transition zone should be highly hydrated (Karato, 2011; Karato et al., 2020; Ohtani et al., 2004; Pearson et al., 2014; Tschauner et al., 2018). The dominant minerals in the mantle transition zone, wadsleyite and ringwoodite, can accommodate up to ~3 wt% H_2O, which is much higher than the H_2O storage capacity of olivine (~0.1 wt%) (Fei & Katsura, 2020; Ferot & Bolfan-Casanova, 2012; Ohtani, 2020). Hence, water is expected to be released when materials from the hydrous mantle transition zone are transported above the 410 km discontinuity via mantle upwelling, triggering partial melting that can be used to explain the low-velocity layer atop 410 km (Han et al., 2020; Yang & Faccenda, 2020). In addition, subducted slabs or stagnant slabs with water stored mainly in hydrous minerals may undergo dehydration reactions and release water that migrates into the overlying mantle wedge or upper mantle (Ohtani & Zhao, 2009; Richard & Iwamori, 2010; Richard et al., 2006; Sheng et al., 2016; Zhao & Ohtani, 2009). While the released water can induce partial melting in the lowermost upper mantle, it can also be re-absorbed by forming phase E according to the previous experimental studies on the phase relations of peridotites (Kawamoto et al., 1995; Komabayashi et al., 2004; Zhang et al., 2019). Based on the results obtained in the present study, the formation of phase E would lead to low V_P and V_S velocities in the regions and thus helps explain the seismic observations of the 410-LVL. Experimental studies on hydrous KLB-1 peridotite have also shown that (Fe, Al)-bearing phase E is stable under the *P–T* conditions along a nearly normal mantle geotherm (Kawamoto et al., 1995; Zhang et al., 2019). The 410-LVLs are characterized by a negative anomaly for both V_P and V_S seismic velocities. A recent seismological study indicated that the seismic anomalies of the 410-LVL beneath the northwest Pacific subduction zone were ~1.0%–1.5% for V_P and ~2.5% for V_S (Han et al., 2020). According to our modeling results on the velocity profiles of phase E and the dry and hydrated pyrolite models, it is estimated that the hydrated pyrolite model containing 13–19 vol% phase E, which corresponds to an H_2O content of 1.5–2.2 wt%, shows a velocity reduction of ~1.0–1.5% for both V_P and V_S relative to the dry pyrolite model. The pyrolite model containing 13–19 vol% phase E can reproduce the observed V_P anomaly of the 410-LVL beneath the northwest Pacific subduction zone; however, it is insufficient to reproduce the observed V_S anomaly. Therefore, the oversimplified model of hydrated pyrolite containing phase E alone cannot explain the genesis of 410-LVL, and other mechanisms, including partial melting that can lead to significantly lower V_S (Berryman, 2000; Hammond & Humphreys, 2000; Karato, 2014; Takei, 2017), should also be taken into consideration.

5. Conclusions

The high *P–T* single-crystal elasticity of phase E has been determined by performing XRD and Brillouin scattering measurements up to 24 GPa and 900 K. Analysis of the obtained single-crystal elasticity data using the third-ordered finite-strain equations allowed us to derive the aggregate elastic parameters of phase E. The adiabatic bulk and shear moduli of phase E under ambient conditions are determined to be $K_{S0} = 98.3(7)$ GPa and $G_0 = 61.0(1)$ GPa, respectively. Their pressure derivatives and temperature derivatives are determined to be $(\partial K_S/\partial P)_T = 5.00(4)$ and $(\partial K_S/\partial T)_P = -0.018(1)$ GPa/K for the adiabatic bulk modulus and $(\partial G/\partial P)_T = 1.64(2)$ and $(\partial G/\partial T)_P = -0.013(2)$ GPa/K for the shear modulus, respectively. Phase E has lower compressional velocity and shear velocity than other relevant or potentially coexisting minerals in the upper mantle and the upper part of the mantle transition zone. Based on the modeled velocity profiles of phase E, dry pyrolite and hydrated (or phase E-bearing) pyrolite models along a slab geotherm 400 K colder than the surrounding mantle, we found that the

existence of phase E would result in low-velocity seismic signatures, implying that phase E is a potential cause for the low-velocity layer atop 410-km depth in some cold and highly-hydrated regions and may also account for some low velocity anomalies in the mantle transition zone.

Data Availability Statement

P–V–T data are listed in Table S1 in Supporting Information S1. Single-crystal and aggregate elastic data are listed in Tables S2 and S3 in Supporting Information S1. Thermoelastic parameters used in the modeling of seismic profiles are given in Table S4 in Supporting Information S1. All these data can also be downloaded online in the Zenodo data repository (https://zenodo.org/record/7243256).

Acknowledgments
This work was financially supported by the Strategic Priority Research Program (B) of the Chinese Academy of Sciences (Grant XDB42000000) and the National Natural Science Foundation of China (Grants 41874107 and 41574079). JFL acknowledges support from the Geophysics Program of the National Science Foundation of the United States (EAR-1916941). The high *P–T* Brillouin and XRD measurements were performed at the 13-BMD and 13-IDD beamlines of GSECARS, APS, Argonne National Laboratory. GSECARS is supported by the National Science Foundation—Earth Sciences (EAR-1634415) and Department of Energy—GeoSciences (DE-FG02–94ER14466). This research used resources of the APS, a U.S. Department of Energy (DOE) Office of Science User Facility operated for the DOE Office of Science by Argonne National Laboratory under Contract No. DE-AC02-06CH11357. This is contribution No. IS-3272 from GIGCAS.

References

Angel, R. J., Gonzalez-Platas, J., & Alvaro, M. (2014). EosFit7c and a Fortran module (library) for equation of state calculations. *Zeitschrift für Kristallographie*, *229*(5), 405–419. https://doi.org/10.1515/zkri-2013-1711

Berryman, J. G. (2000). Seismic velocity decrement ratios for regions of partial melt in the lower mantle. *Geophysical Research Letters*, *27*(3), 421–424. https://doi.org/10.1029/1999gl008402

Birch, F. (1947). Finite elastic strain of cubic crystals. *Physical Review*, *71*(11), 809–824. https://doi.org/10.1103/physrev.71.809

Birch, F. (1978). Finite strain isotherm and velocities for single-crystal and polycrystalline NaCl at high pressure and 300 K. *Journal of Geophysical Research*, *83*(B3), 1257–1268. https://doi.org/10.1029/jb083ib03p01257

Chang, S. J., & Ferreira, A. M. (2019). Inference on water content in the mantle transition zone near subducted slabs from anisotropy tomography. *Geochemistry, Geophysics, Geosystems*, *20*(2), 1189–1201. https://doi.org/10.1029/2018gc008090

Crichton, W. A., & Ross, N. L. (2000). Equation of state of phase E. *Mineralogical Magazine*, *64* (3), 561–567. https://doi.org/10.1180/002646100549427

Duan, Y., Sun, N., Wang, S., Li, X., Guo, X., Ni, H., et al. (2018). Phase stability and thermal equation of state of δ-AlOOH: Implication for water transportation to the Deep Lower Mantle. *Earth and Planetary Science Letters*, *494*, 92–98. https://doi.org/10.1016/j.epsl.2018.05.003

Duffy, T. S., & Anderson, D. L. (1989). Seismic velocities in mantle minerals and the mineralogy of the upper mantle. *Journal of Geophysical Research*, *94*(B2), 1895–1912. https://doi.org/10.1029/jb094ib02p01895

Dziewonski, A. M., & Anderson, D. L. (1981). Preliminary reference Earth model. *Physics of the Earth and Planetary Interiors*, *25*(4), 297–356. https://doi.org/10.1016/0031-9201(81)90046-7

Every, A. (1980). General closed-form expressions for acoustic waves in elastically anisotropic solids. *Physical Review B*, *22*(4), 1746–1760. https://doi.org/10.1103/physrevb.22.1746

Fan, D., Fu, S., Lu, C., Xu, J., Zhang, Y., Tkachev, S. N., et al. (2020). Elasticity of single-crystal Fe-enriched diopside at high-pressure conditions: Implications for the origin of upper mantle low-velocity zones. *American Mineralogist*, *105*(3), 363–374. https://doi.org/10.2138/am-2020-7075

Fan, D., Fu, S., Yang, J., Tkachev, S. N., Prakapenka, V. B., & Lin, J.-F. (2019). Elasticity of single-crystal periclase at high pressure and temperature: The effect of iron on the elasticity and seismic parameters of ferropericlase in the lower mantle. *American Mineralogist*, *104*(2), 262–275. https://doi.org/10.2138/am-2019-6656

Fei, H., & Katsura, T. (2020). High water solubility of ringwoodite at mantle transition zone temperature. *Earth and Planetary Science Letters*, *531*, 115987. https://doi.org/10.1016/j.epsl.2019.115987

Fei, Y., Ricolleau, A., Frank, M., Mibe, K., Shen, G., & Prakapenka, V. (2007). Toward an internally consistent pressure scale. *Proceedings of the National Academy of Sciences*, *104*(22), 9182–9186. https://doi.org/10.1073/pnas.0609013104

Ferot, A., & Bolfan-Casanova, N. (2012). Water storage capacity in olivine and pyroxene to 14 GPa: Implications for the water content of the Earth's upper mantle and nature of seismic discontinuities. *Earth and Planetary Science Letters*, *349*, 218–230. https://doi.org/10.1016/j.epsl.2012.06.022

Frost, D. J., & Fei, Y. W. (1998). Stability of phase D at high pressure and high temperature. *Journal of Geophysical Research*, *103*(B4), 7463–7474. https://doi.org/10.1029/98jb00077

Fu, S., Yang, J., & Lin, J.-F. (2017). Abnormal elasticity of single-crystal magnesiosiderite across the spin transition in Earth's lower mantle. *Physical Review Letters*, *118*(3), 036402. https://doi.org/10.1103/physrevlett.118.036402

Fu, S., Yang, J., Tsujino, N., Okuchi, T., Purevjav, N., & Lin, J.-F. (2019). Single-crystal elasticity of (Al, Fe)-bearing bridgmanite and seismic shear wave radial anisotropy at the topmost lower mantle. *Earth and Planetary Science Letters*, *518*, 116–126. https://doi.org/10.1016/j.epsl.2019.04.023

Hammond, W. C., & Humphreys, E. D. (2000). Upper mantle seismic wave velocity' effects of realistic partial melt geometries. *Jounal of Geophysical Research*, *105*(B5), 10975–10986. https://doi.org/10.1029/2000jb900041

Han, G., Li, J., Guo, G., Mooney, W. D., Karato, S.-i., & Yuen, D. A. (2020). Pervasive low-velocity layer atop the 410-km discontinuity beneath the northwest Pacific subduction zone: Implications for rheology and geodynamics. *Earth and Planetary Science Letters*, *554*, 116642. https://doi.org/10.1016/j.epsl.2020.116642

Hao, M., Zhang, J. S., Pierotti, C. E., Zhou, W.-Y., Zhang, D., & Dera, P. (2020). The seismically fastest chemical heterogeneity in the Earth's deep upper mantle—Implications from the single-crystal thermoelastic properties of jadeite. *Earth and Planetary Science Letters*, *543*, 116345. https://doi.org/10.1016/j.epsl.2020.116345

Hill, R. (1952). The elastic behaviour of a crystalline aggregate. *Proceedings of the Physical Society Section A*, *65*(5), 349–354. https://doi.org/10.1088/0370-1298/65/5/307

Holland, T., & Redfern, S. (1997). UNITCELL: A nonlinear least-squares program for cell-parameter refinement and implementing regression and deletion diagnostics. *Journal of Applied Crystallography*, *30*(1), 84. https://doi.org/10.1107/s0021889896011673

Irifune, T., Higo, Y., Inoue, T., Kono, Y., Ohfuji, H., & Funakoshi, K. (2008). Sound velocities of majorite garnet and the composition of the mantle transition region. *Nature*, *451*(7180), 814–817. https://doi.org/10.1038/nature06551

Irifune, T., & Isshiki, M. (1998). Iron partitioning in a pyrolite mantle and the nature of the 410-km seismic discontinuity. *Nature*, *392*(6677), 702–705. https://doi.org/10.1038/33663

Isaak, D., Ohno, I., & Lee, P. (2006). The elastic constants of monoclinic single-crystal chrome-diopside to 1, 300 K. *Physics and Chemistry of Minerals*, *32*(10), 691–699. https://doi.org/10.1007/s00269-005-0047-9

Isaak, D. G., Gwanmesia, G. D., Davis, M. G., Stafford, S. C., Stafford, A. M., & Triplett, R. S. (2010). The temperature dependence of the elasticity of Fe-bearing wadsleyite. *Physics of the Earth and Planetary Interiors*, *182*(1–2), 107–112. https://doi.org/10.1016/j.pepi.2010.06.014

Ishii, T., Kojitani, H., & Akaogi, M. (2011). Post-spinel transitions in pyrolite and Mg_2SiO_4 and akimotoite-perovskite transition in $MgSiO_3$: Precise comparison by high-pressure high-temperature experiments with multi-sample cell technique. *Earth and Planetary Science Letters*, *309*(3–4), 185–197. https://doi.org/10.1016/j.epsl.2011.06.023

Iwamori, H. (2004). Phase relations of peridotites under H_2O-saturated conditions and ability of subducting plates for transportation of H_2O. *Earth and Planetary Science Letters*, *227*(1–2), 57–71. https://doi.org/10.1016/j.epsl.2004.08.013

Kantor, I., Prakapenka, V., Kantor, A., Dera, P., Kurnosov, A., Sinogeikin, S., et al. (2012). BX90: A new diamond anvil cell design for X-ray diffraction and optical measurements. *Review of Scientific Instruments*, *83*(12), 125102–125106. https://doi.org/10.1063/1.4768541

Kanzaki, M. (1991). Stability of hydrous magnesium silicates in the mantle transition zone. *Physics of the Earth and Planetary Interiors*, *66*(3–4), 307–312. https://doi.org/10.1016/0031-9201(91)90085-v

Karato, S.-i. (2011). Water distribution across the mantle transition zone and its implications for global material circulation. *Earth and Planetary Science Letters*, *301*(3–4), 413–423. https://doi.org/10.1016/j.epsl.2010.11.038

Karato, S.-i. (2014). Does partial melting explain geophysical anomalies? *Physics of the Earth and Planetary Interiors*, *228*, 300–306. https://doi.org/10.1016/j.pepi.2013.08.006

Karato, S.-i., Karki, B., & Park, J. (2020). Deep mantle melting, global water circulation and its implications for the stability of the ocean mass. *Progress in Earth and Planetary Science*, *7*(1), 1–25. https://doi.org/10.1186/s40645-020-00379-3

Karki, B., Stixrude, L., & Wentzcovitch, R. (2001). High-pressure elastic properties of major materials of Earth's mantle from first principles. *Reviews of Geophysics*, *39*(4), 507–534. https://doi.org/10.1029/2000RG000088

Katsura, T., Shatskiy, A., Manthilake, M. G. M., Zhai, S., Yamazaki, D., Matsuzaki, T., et al. (2009). P-V-T relations of wadsleyite determined by in situ X-ray diffraction in a large-volume high-pressure apparatus. *Geophysical Research Letters*, *36*(11), L11307. https://doi.org/10.1029/2009gl038107

Katsura, T., Yoneda, A., Yamazaki, D., Yoshino, T., & Ito, E. (2010). Adiabatic temperature profile in the mantle. *Physics of the Earth and Planetary Interiors*, *183*(1–2), 212–218. https://doi.org/10.1016/j.pepi.2010.07.001

Kawamoto, T., Leinenweber, K., Hervig, R. L., & Holloway, J. R. (1995). Stability of hydrous minerals in H_2O-saturated KLB-1 peridotite up to 15 GPa. In *AIP Conference Proceedings* (Vol. 341, pp. 229–239). American Institute of Physics.

Kennett, B. L., Engdahl, E., & Buland, R. (1995). Constraints on seismic velocities in the Earth from traveltimes. *Geophysical Journal International*, *122*(1), 108–124. https://doi.org/10.1111/j.1365-246x.1995.tb03540.x

Komabayashi, T., Omori, S., & Maruyama, S. (2004). Petrogenetic grid in the system MgO-SiO_2-H_2O up to 30 GPa, 1600°C: Applications to hydrous peridotite subducting into the Earth's deep interior. *Journal of Geophysical Research*, *109*(B3), B03206. https://doi.org/10.1029/2003JB002651

Kudoh, Y., Finger, L., Hazen, R., Prewitt, C., Kanzaki, M., & Veblen, D. (1993). Phase E: A high pressure hydrous silicate with unique crystal chemistry. *Physics and Chemistry of Minerals*, *19*(6), 357–360. https://doi.org/10.1007/bf00202972

Kuritani, T., Xia, Q.-K., Kimura, J.-I., Liu, J., Shimizu, K., Ushikubo, T., et al. (2019). Buoyant hydrous mantle plume from the mantle transition zone. *Scientific Reports*, *9*(1), 1–7. https://doi.org/10.1038/s41598-019-43103-y

Lee, C. T. A. (2003). Compositional variation of density and seismic velocities in natural peridotites at STP conditions: Implications for seismic imaging of compositional heterogeneities in the upper mantle. *Journal of Geophysical Research*, *108*(B9), 2441. https://doi.org/10.1029/2003JB002413

Li, G. H., Gao, Y., Zhou, Y. Z., Ju, C. H., Shi, Y. T., & Cui, Q. H. (2022). A low-velocity layer atop the mantle transition zone beneath the Western Central Asian Orogenic Belt: Upper mantle melting induced by ancient slab subduction. *Earth and Planetary Science Letters*, *578*, 11728. https://doi.org/10.1016/j.epsl.2021.117287

Li, X., Mao, Z., Sun, N., Liao, Y., Zhai, S., Wang, Y., et al. (2016). Elasticity of single-crystal superhydrous phase B at simultaneous high pressure-temperature conditions. *Geophysical Research Letters*, *43*(16), 8458–8465. https://doi.org/10.1002/2016gl070027

Lin, J.-F., Mao, Z., Yang, J., & Fu, S. (2018). Elasticity of lower-mantle bridgmanite. *Nature*, *564*(7736), E18–E26. https://doi.org/10.1038/s41586-018-0741-7

Litasov, K., & Ohtani, E. (2003). Stability of various hydrous phases in CMAS pyrolite-H_2O system up to 25 GPa. *Physics and Chemistry of Minerals*, *30*(3), 147–156. https://doi.org/10.1007/s00269-003-0301-y

Lu, C., Mao, Z., Lin, J. F., Zhuravlev, K. K., Tkachev, S. N., & Prakapenka, V. B. (2013). Elasticity of single-crystal iron-bearing pyrope up to 20 GPa and 750 K. *Earth and Planetary Science Letters*, *361*, 134–142. https://doi.org/10.1016/j.epsl.2012.11.041

Mainprice, D., Barruol, G., & Ismaïl, W. B. (2000). The seismic anisotropy of the Earth's mantle: From single crystal to polycrystal. In S.-I. Karato, A. Forte, R. Liebermann, G. Masters, & L. Stixrude (Eds.), *Earth's deep interior: Mineral Physics and tomography from the atomic to the global scale* (Vol. 117, pp. 237–264). AGU. https://doi.org/10.1029/GM117p0237

Mao, Z., Fan, D., Lin, J.-F., Yang, J., Tkachev, S. N., Zhuravlev, K., & Prakapenka, V. B. (2015). Elasticity of single-crystal olivine at high pressures and temperatures. *Earth and Planetary Science Letters*, *426*, 204–215. https://doi.org/10.1016/j.epsl.2015.06.045

Mookherjee, M., & Tsuchiya, J. (2015). Elasticity of superhydrous phase, B, $Mg_{10}Si_3O_{14}(OH)_4$. *Physics of the Earth and Planetary Interiors*, *238*, 42–50. https://doi.org/10.1016/j.pepi.2014.10.010

Murakami, M., Sinogeikin, S. V., Litasov, K., Ohtani, E., & Bass, J. D. (2008). Single-crystal elasticity of iron-bearing majorite to 26 GPa: Implications for seismic velocity structure of the mantle transition zone. *Earth and Planetary Science Letters*, *274*(3–4), 339–345. https://doi.org/10.1016/j.epsl.2008.07.045

Nishihara, Y., Takahashi, E., Matsukage, K. N., Iguchi, T., Nakayama, K., & Funakoshi, K. (2003). Thermal equation of state of (Mg0.91Fe0.09)-$2SiO_4$ ringwoodite. *Physics of the Earth and Planetary Interiors*, *143*(144), 33–46. https://doi.org/10.1016/j.pepi.2003.02.001

Nye, J. F. (1985). *Physical properties of crystals: Their representation by tensors and matrices*. Oxford University Press.

Obayashi, M., Sugioka, H., Yoshimitsu, J., & Fukao, Y. (2006). High temperature anomalies oceanward of subducting slabs at the 410-km discontinuity. *Earth and Planetary Science Letters*, *243*(1–2), 149–158. https://doi.org/10.1016/j.epsl.2005.12.032

Ohtani, E. (2020). The role of water in Earth's mantle. *National Science Review*, *7*(1), 224–232. https://doi.org/10.1093/nsr/nwz071

Ohtani, E., Litasov, K., Hosoya, T., Kubo, T., & Kondo, T. (2004). Water transport into the deep mantle and formation of a hydrous transition zone. *Physics of the Earth and Planetary Interiors*, *143*, 255–269. https://doi.org/10.1016/j.pepi.2003.09.015

Ohtani, E., & Zhao, D. (2009). The role of water in the deep upper mantle and transition zone: Dehydration of stagnant slabs and its effects on the big mantle wedge. *Russian Geology and Geophysics*, *50*(12), 1073–1078. https://doi.org/10.1016/j.rgg.2009.11.006

Pandolfo, F., Cámara, F., Domeneghetti, M. C., Alvaro, M., Nestola, F., Karato, S.-I., & Amulele, G. (2015). Volume thermal expansion along the jadeite–diopside join. *Physics and Chemistry of Minerals*, *42*(1), 1–14. https://doi.org/10.1007/s00269-014-0694-9

Pearson, D., Brenker, F., Nestola, F., McNeill, J., Nasdala, L., Hutchison, M., et al. (2014). Hydrous mantle transition zone indicated by ringwoodite included within diamond. *Nature*, *507*(7491), 221–224. https://doi.org/10.1038/nature13080

Prescher, C., & Prakapenka, V. B. (2015). DIOPTAS: A program for reduction of two-dimensional X-ray diffraction data and data exploration. *High Pressure Research*, *35*(3), 223–230. https://doi.org/10.1080/08957959.2015.1059835

Purevjav, N., Okuchi, T., & Hoffmann, C. (2020). Strong hydrogen bonding in a dense hydrous magnesium silicate discovered by neutron Laue diffraction. *IUCrJ*, *7*(3), 370–374. https://doi.org/10.1107/s2052252520003036

Revenaugh, J., & Sipkin, S. A. (1994). Seismic evidence for silicate melt atop the 410 km mantle discontinuity. *Nature*, *369*(6480), 474–476. https://doi.org/10.1038/369474a0

Richard, G., Bercovici, D., & Karato, S. I. (2006). Slab dehydration in the Earth's mantle transition zone. *Earth and Planetary Science Letters*, *251*(1–2), 156–167. https://doi.org/10.1016/j.epsl.2006.09.006

Richard, G., & Iwamori, H. (2010). Stagnant slab, wet plumes and Cenozoic volcanism in East Asia. *Physics of the Earth and Planetary Interiors*, *183*(1–2), 280–287. https://doi.org/10.1016/j.pepi.2010.02.009

Rosa, A. D., Sanchez-Valle, C., & Ghosh, S. (2012). Elasticity of phase D and implication for the degree of hydration of deep subducted slabs. *Geophysical Research Letters*, *39*(6), L06304. https://doi.org/10.1029/2012GL050927

Sanchez-Valle, C., Wang, J., & Rohrbach, A. (2019). Effect of calcium on the elasticity of majoritic garnets and the seismic gradients in the mantle transition zone. *Physics of the Earth and Planetary Interiors*, *293*, 106272. https://doi.org/10.1016/j.pepi.2019.106272

Satta, N., Marquardt, H., Kurnosov, A., Buchen, J., Kawazoe, T., McCammon, C., & Ballaran, T. B. (2019). Single-crystal elasticity of iron-bearing phase E and seismic detection of water in Earth's upper mantle. *American Mineralogist*, *104*(10), 1526–1529. https://doi.org/10.2138/am-2019-7084

Schmidt, M. W., & Poli, S. (1998). Experimentally based water budgets for dehydrating slabs and consequences for arc magma generation. *Earth and Planetary Science Letters*, *163*(1–4), 361–379. https://doi.org/10.1016/s0012-821x(98)00142-3

Sheng, J., Liao, J., & Gerya, T. (2016). Numerical modeling of deep oceanic slab dehydration: Implications for the possible origin of far field intra-continental volcanoes in northeastern China. *Journal of Asian Earth Sciences*, *117*, 328–336. https://doi.org/10.1016/j.jseaes.2015.12.022

Shieh, S. R., Mao, H.-k., Konzett, J. r., & Hemley, R. J. (2000). In-situ high pressure X-ray diffraction of phase E to 15 GPa. *American Mineralogist*, *85*(5–6), 765–769. https://doi.org/10.2138/am-2000-5-616

Sinogeikin, S., Bass, J., Prakapenka, V., Lakshtanov, D., Shen, G., Sanchez-Valle, C., & Rivers, M. (2006). Brillouin spectrometer interfaced with synchrotron radiation for simultaneous X-ray density and acoustic velocity measurements. *Review of Scientific Instruments*, *77*(10), 103905. https://doi.org/10.1063/1.2360884

Stixrude, L., & Lithgow-Bertelloni, C. (2005). Thermodynamics of mantle minerals—I. Physcial properties. *Geophysical Journal International*, *162*, 610–632. https://doi.org/10.1111/j.1365-246X.2005.02642.x

Sun, Y., Hier-Majumder, S., Xu, Y., & Walter, M. (2020). Stability and migration of slab-derived carbonate-rich melts above the transition zone. *Earth and Planetary Science Letters*, *531*, 116000. https://doi.org/10.1016/j.epsl.2019.116000

Takei, Y. (2017). Effects of partial melting on seismic velocity and attenuation: A new insight from experiments. *Annual Review of Earth and Planetary Sciences*, *45*(1), 447–470. https://doi.org/10.1146/annurev-earth-063016-015820

Tang, Y., Obayashi, M., Niu, F., Grand, S. P., Chen, Y. J., Kawakatsu, H., et al. (2014). Changbaishan volcanism in northeast China linked to subduction-induced mantle upwelling. *Nature Geoscience*, *7*(6), 470–475. https://doi.org/10.1038/ngeo2166

Tauzin, B., Debayle, E., & Wittlinger, G. (2010). Seismic evidence for a global low-velocity layer within the Earth's upper mantle. *Nature Geoscience*, *3*(10), 718–721. https://doi.org/10.1038/ngeo969

Tauzin, B., Kim, S., & Kennett, B. (2017). Pervasive seismic low-velocity zones within stagnant plates in the mantle transition zone: Thermal or compositional origin? *Earth and Planetary Science Letters*, *477*, 1–13. https://doi.org/10.1016/j.epsl.2017.08.006

Thomson, A. R., Walter, M. J., Kohn, S. C., & Brooker, R. A. (2016). Slab melting as a barrier to deep carbon subduction. *Nature*, *529*(7584), 76–79. https://doi.org/10.1038/nature16174

Tomioka, N., Okuchi, T., Purevjav, N., Abe, J., & Harjo, S. (2016). Hydrogen sites in the dense hydrous magnesian silicate phase E: A pulsed neutron powder diffraction study. *Physics and Chemistry of Minerals*, *43*(4), 267–275. https://doi.org/10.1007/s00269-015-0791-4

Tschauner, O., Huang, S., Greenberg, E., Prakapenka, V., Ma, C., Rossman, G., et al. (2018). Ice-VII inclusions in diamonds: Evidence for aqueous fluid in Earth's deep mantle. *Science*, *359*(6380), 1136–1139. https://doi.org/10.1126/science.aao3030

Tsuchiya, J., & Tsuchiya, T. (2008). Elastic properties of phase D ($MgSi_2O_6H_2$) under pressure: Ab initio investigation. *Physics of the Earth and Planetary Interiors*, *170*(3–4), 215–220. https://doi.org/10.1016/j.pepi.2008.05.015

Vinnik, L., & Farra, V. (2007). Low S velocity atop the 410-km discontinuity and mantle plumes. *Earth and Planetary Science Letters*, *262*(3–4), 398–412. https://doi.org/10.1016/j.epsl.2007.07.051

Wang, B. Y., Zhang, Y. Y., Fu, S. Y., Yan, W., Takahashi, E., Li, L., et al. (2022). Single-crystal elasticity of phase Egg $AlSiO_3OH$ and delta-AlOOH by Brillouin spectroscopy. *American Mineralogist*, *107*(1), 147–152. https://doi.org/10.2138/am-2022-8056

Wang, J., Bass, J. D., & Kastura, T. (2014). Elastic properties of iron-bearing wadsleyite to 17.7 GPa: Implications for mantle mineral models. *Physics of the Earth and Planetary Interiors*, *228*, 92–96. https://doi.org/10.1016/j.pepi.2014.01.015

Wei, S. S., & Shearer, P. M. (2017). A sporadic low-velocity layer atop the 410 km discontinuity beneath the Pacific Ocean. *Journal of Geophysical Research: Solid Earth*, *122*(7), 5144–5159. https://doi.org/10.1002/2017jb014100

Xu, C., Gréaux, S., Inoue, T., Noda, M., Sun, W., Kuwahara, H., & Higo, Y. (2020). Sound velocities of Al-bearing phase D up to 22 GPa and 1300 K. *Geophysical Research Letters*, *47*(18), e2020GL088877. https://doi.org/10.1029/2020gl088877

Yang, J., & Faccenda, M. (2020). Intraplate volcanism originating from upwelling hydrous mantle transition zone. *Nature*, *579*(7797), 88–91. https://doi.org/10.1038/s41586-020-2045-y

Yang, J., Lin, J. F., Jacobsen, S. D., Seymour, N. M., Tkachev, S. N., & Prakapenka, V. B. (2016). Elasticity of ferropericlase and seismic heterogeneity in the Earth's lower mantle. *Journal of Geophysical Research: Solid Earth*, *121*(12), 8488–8500. https://doi.org/10.1002/2016jb013352

Yang, J., Mao, Z., Lin, J. F., & Prakapenka, V. B. (2014). Single-crystal elasticity of the deep-mantle magnesite at high pressure and temperature. *Earth and Planetary Science Letters*, *392*, 292–299. https://doi.org/10.1016/j.epsl.2014.01.027

Zhang, J. S., Bass, J. D., & Schmandt, B. (2018). The elastic anisotropy change near the 410-km discontinuity: Predictions from single-crystal elasticity measurements of olivine and wadsleyite. *Journal of Geophysical Research: Solid Earth*, *123*(4), 2674–2684. https://doi.org/10.1002/2017jb015339

Zhang, J. Z., & Kostak, P., Jr. (2002). Thermal equation of state of magnesiowüstite ($Mg_{0.6}Fe_{0.4}$)O. *Physics of the Earth and Planetary Interiors*, *129*(3–4), 301–311. https://doi.org/10.1016/s0031-9201(01)00296-5

Zhang, L., Smyth, J. R., Kawazoe, T., Jacobsen, S. D., Niu, J., He, X., & Qin, S. (2019). Stability, composition, and crystal structure of Fe-bearing Phase E in the transition zone. *American Mineralogist*, *104*(11), 1620–1624. https://doi.org/10.2138/am-2019-6750

Zhang, Y., Fu, S., Wang, B., & Lin, J.-F. (2021). Elasticity of a pseudoproper ferroelastic transition from Stishovite to post-Stishovite at high pressure. *Physical Review Letters*, *126*(2), 025701. https://doi.org/10.1103/physrevlett.126.025701

Zhao, D., & Ohtani, E. (2009). Deep slab subduction and dehydration and their geodynamic consequences: Evidence from seismology and mineral physics. *Gondwana Research*, *16*(3–4), 401–413. https://doi.org/10.1016/j.gr.2009.01.005

Zou, Y., Gréaux, S., Irifune, T., Whitaker, M. L., Shinmei, T., & Higo, Y. (2012). Thermal equation of state of $Mg_3 Al_2 Si_3 O_{12}$ pyrope garnet up to 19 GPa and 1, 700 K. *Physics and Chemistry of Minerals*, *39*(7), 589–598. https://doi.org/10.1007/s00269-012-0514-z